Supplementary Material for:

The influence of river-derived particles on estuarine and marine elemental cycles: evidence from lithium isotopes

Authors: Chun-Yao Liu[a]*, David J. Wilson[a], Ed C. Hathorne[b], Antao Xu[b], Philip A. E. Pogge von Strandmann[a,c]

[a] London Geochemistry and Isotope Centre (LOGIC), Institute of Earth and Planetary Sciences, University College London and Birkbeck, University of London, Gower Street, London WC1E 6BT, UK

[b] GEOMAR Helmholtz Centre for Ocean Research Kiel, Wischhofstrasse 1-3, Kiel 24148, Germany

[c] Mainz Isotope Geochemistry (MIGHTY), Institute of Geosciences, Johannes Gutenberg University, 55122, Mainz, Germany

* Corresponding author. e-mail: chunyao.liu.19@ucl.ac.uk

S1. Comparison of bulk elemental compositions obtained by different methods (calculation vs. measurement).

The MUC samples in this study are the uppermost 0.5–2 cm of sediment for each core at sampling locations from the GEOTRACES M147 cruise. The M147 cruise also obtained sediment samples at different depths of more than one core at each sampling location for other scientific topics (Koschinsky et al., 2018, Spiegel et al., 2021, Vosteen et al., 2022). Using these samples, Spiegel et al. (2021) obtained the concentrations of Li, Ca, Mg, K, Fe, Mn and Al of MUC24, MUC41, MUC67, MUC73, MUC85, MUC89, MUC93, MUC108 and MUC117 by ICP-OES after dissolving bulk samples in HF-$HClO_4$-HNO_3, and Vosteen et al. (2022) obtained the concentrations of K, Fe, and Al of MUC24, MUC41, MUC85, MUC89, MUC93 and MUC117 by ICP-OES after dissolving bulk samples in HF-$HClO_4$-HNO_3. Here, the average elemental compositions of the sediments at 0–1 cm and 1–2 cm from Spiegel et al. (2021) and Vosteen et al. (2022) are compared with the bulk elemental compositions calculated based on the chemical extraction data in this study.

The relative standard deviations (RSD) between $[Li]_{bulk}$ from this study and the measured bulk Li concentrations (Spiegel et al., 2021) are 1.0% to 22.9% (4 samples < 5%; 4 samples at 5–15%; 1 sample at 22.9%). The average RSD between the concentrations of Ca, Mg, K, Fe, Mn and Al in the bulk samples obtained in this study and in Spiegel et al. (2021) are 20%, 18%, 10%, 8%, 11% and 20%, respectively. The RSD between the concentrations of K, Fe and Al in the bulk samples obtained in this study and Vosteen et al. (2022) are 0.9–28.0% (mostly 0.9–3.8%, plus only one at 28.0%), 0.1–7.6% and 1.4–8.9%, respectively. The differences may be due to analytical precision and/or natural variability due to differences between sampled cores

during the GEOTRACES M147 cruise, where more than one core was collected at each sampling site (Koschinsky et al., 2018).

S2. The chemical extracted phases of the sediments

S2.1 Influence of the remaining dissolved load on the exchangeable pool

The process of sampling and the existence of pore water could potentially influence the suspended load sediment (SPM) and/or surface sediment (MUC) samples. The river water or seawater may attach to the SPM and MUC samples, although both the MUC and SPM samples were separated by centrifugation before freeze drying (Section 2.2) (Koschinsky et al., 2018). Theoretically, some of the elements in this dissolved material could remain in the SPM and MUC samples, and would likely be re-dissolved in the leachates of the first phase (i.e., exchangeable pool).

Based on the elemental concentrations of the dissolved load samples from the Amazon south channel transect, the Ca/Li, Mg/Li and K/Li ratios of the riverine endmember are 6.9, 3.5 and 1.9 g/mg, respectively, and these ratios are 2.4, 7.3 and 2.4 g/mg in seawater. The δ^7Li value of the riverine endmember is 23.7‰, and in saline water it ranges from 29.4–32.8‰. Basically, the Ca/Li, Mg/Li, and K/Li ratios in the pore water of the ocean surface sediments are similar to the overlying saline water (Smrzka et al., 2019; Andrews et al., 2020). Previous studies also confirm that Li concentrations and isotope compositions in the pore waters of surface ocean sediments are similar to seawater (Zhang et al., 1998; Andrews et al., 2020). In contrast, the $[Ca]_{exchangeable}/[Li]_{exchangeable}$, $[Mg]_{exchangeable}/[Li]_{exchangeable}$ and $[K]_{exchangeable}/[Li]_{exchangeable}$ ratios of both the SPM and MUC samples do not exhibit typical seawater

elemental ratios or a binary mixing trend between seawater and clay compositions (Fig. S1) (Yang et al., 2021). Furthermore, the SPM samples from the Amazon north channel fit the trend of the MUC samples from the Amazon north channel transect (Fig. S1), even though the SPM and MUC samples were sampled and treated by different methods in the field (Section 2.2). In addition, two SPM samples (SPM8s and SPM8d) are from the same location but different water depths, and therefore different salinities (20 and 24, respectively), yet show similar $[Ca]_{exchangeable}$, $[Mg]_{exchangeable}$, $[K]_{exchangeable}$, $[Li]_{exchangeable}$ and $\delta^7Li_{exchangeable}$ (Table 2). The $[Ca]_{exchangeable}$, $[Mg]_{exchangeable}$ and $[K]_{exchangeable}$ values are within the ranges of concentrations of exchangeable Ca, Mg and K in of Sayles and Mangelsdorf (1979). The above evidence therefore supports that any remaining ambient waters (i.e., saline water and/or pore water) have a negligible influence on the extracted exchangeable pool.

S2.2 Elemental concentrations in exchangeable pool

Apart from Na, which was added from the leaching reagents (NaOAc), the exchangeable pool of both SPM and MUC samples are dominated by Mg, Ca and K, whereas the Fe, Al and Mn contents are very low (Fig. S2, Table 2 in main text). In the north channel transect, the $[Ca]_{exchangeable}$ fluctuates from 0.68 to 0.85 mg/g at low and medium salinity and increases to 1.54 mg/g at high salinity. The $[Mg]_{exchangeable}$ increases from 0.51 mg/g in the river endmember to 1.17 mg/g at low salinity, and then fluctuates from 1.16 to 1.41 mg/g at higher salinities. The $[K]_{exchangeable}$ generally increases through the transect from 0.12 to 1.06 mg/g. In the alongshore transect, $[K]_{exchangeable}$ generally remains constant, whereas $[Ca]_{exchangeable}$ and $[Mg]_{exchangeable}$ increase from 0.81 to 1.63 mg/g, and from 1.39 to 1.87 mg/g, respectively.

S2.3. Influences on carbonate leachates

The sample 41MUC contains 39.7% carbonate, based on the total inorganic carbonate analysis (Spiegel et al., 2021). Its $[Ca]_{carbonate}$ is 66.9 mg/g, which is around 80 times higher than its $[Mg]_{carbonate}$, which indicates that calcium carbonate dominates its carbonate leachates. The $[Mn]_{carbonate}/[Ca]_{carbonate}$ and $[Al]_{carbonate}/[Ca]_{carbonate}$ ratios are 0.30 mg/g and 0.13 mg/g, respectively. Furthermore, the $[Ca]_{oxide}$ of 41MUC is 120 mg/g, which is higher than its $[Ca]_{carbonate}$, indicating that the oxide leachates of 41MUC are likely to be influenced by carbonates that were not fully leached in the previous step. This scenario likely arises because our leaching method is primarily designed for silicate soils, sediments and rocks, with carbonate contents at least less than 15% and ideally less than 5% (Liu et al., 2022). The $[Li]_{carbonate}$ of 41MUC is 0.33 μg/g, which represents only approximately 1% of the Li in the bulk sample, while the $\delta^7Li_{carbonate}$ value of 41MUC is 14.9‰.

Apart from sample 41MUC, the operationally-defined carbonate leachates of the other MUC and SPM samples are likely to be partly influenced by leaching of other phases, due to their low carbonate contents. Most of the suspended particles transported by the Amazon river to the estuary are derived from the Andes mountains, where the rocks rarely contain carbonates (Gibbs, 1967; Kuehl et al., 1982; Baturin and Gordeev, 2019). Furthermore, the calculated saturation index (SI) of carbonates in the river endmember (W66) and the pH of the Amazon mainstream of around 6.8 indicate that carbonate precipitation is not favourable in this river system (Fig. S5) (Dellinger et al., 2015).

The $[Ca]_{carbonate}/[Mg]_{carbonate}$ and $[Ca]_{carbonate}/[Ca]_{exchangeable}$ ratios of the sediment samples

(except 41MUC) range from 0.6 to 8.7 and from 0.25 to 3.85, respectively, without clear trends. These data indicate a lack of significant calcium carbonate content in these sediments, and therefore clays may influence the carbonate leachates (Liu et al., 2022). Furthermore, except for sample 41MUC, the $[Mn]_{carbonate}/[Ca]_{carbonate}$ ratios range from 34 to 253 mg/g, and $[Al]_{carbonate}/[Ca]_{carbonate}$ ratios range from 4 to 118 mg/g. In contrast, the Mn/Ca ratios in leachates of carbonate-dominated samples range from 0.1 μg/g to 35 mg/g (Misra and Froelich, 2012; Pogge Von Strandmann et al., 2013, 2019b, 2021; Ullmann et al., 2013; Bastian et al., 2018; Dellinger et al., 2020; Washington et al., 2020), while the recommended Al/Ca ratios in carbonate leachates should be less than 0.54 mg/g (i.e., 0.8 mmol/mol) (Pogge Von Strandmann et al., 2013) or even less than 0.27 mg/g (i.e., 0.4 mmol/mol) (Dellinger et al., 2020). Except for 41MUC, the $\delta^7Li_{carbonate}$ values of the other sediments lie between their corresponding $\delta^7Li_{exchangeable}$ and δ^7Li_{oxide} values (Fig. 3 in main text). The above evidence suggests that, when the carbonate content in the sediments is low (Spiegel et al., 2021), the operationally-defined carbonate leachates are probably not dominated by carbonate, but may be influenced by the dissolution of other phases instead (Liu et al., 2022).

S2.4 Oxide leachates

The oxide leachate of 41MUC is likely influenced by additional leaching of carbonate remaining from the previous step due to its high carbonate content (Supplementary Material S2.3). For all other samples, Fe, Mn and Al dominate the oxide leachates of the MUC and SPM samples (Fig. S2). For example, $[Ca]_{oxide}/[Fe]_{oxide}$, $[Mg]_{oxide}/[Fe]_{oxide}$, and $[K]_{oxide}/[Fe]_{oxide}$ of the sediments range from 0.13–0.41 g/g, 0.05–0.17 g/g, and 0.02–0.18 g/g, respectively.

However, it is difficult to completely avoid interference from clay phases (Supplementary Material S3; Liu et al., 2022). In that context, it is worth noting that $[Mg]_{oxide}$ and $[K]_{oxide}$, which usually enter clays instead of oxides, increase with salinity in the Amazon north channel transect from 0.02 to 0.2 mg/g and from 0.02 to 0.14 mg/g, respectively.

In the north channel transect, $[Fe]_{oxide}$ generally increases from 0.47 to 1.53 mg/g with salinity (Fig. S2). Meanwhile, $[Fe]_{oxide}/[Fe]_{bulk}$ fluctuates at around 1.5% from the river endmember up to medium salinity, then increases to 3.6% at a salinity of ~20. In the alongshore transect, $[Fe]_{oxide}$ remains stable at around 1.0 mg/g. For $[Mn]_{oxide}$, one ocean surface sediment sample, 85MUC, located at the intersection of the north channel transect and the alongshore transect has low $[Mn]_{oxide}$ (0.03 mg/g). Except for 85MUC and 41MUC, the $[Mn]_{oxide}$ in the north transect varies in a narrow range from 0.17 to 0.24 mg/g; these values are higher than $[Mg]_{oxide}$ and $[K]_{oxide}$ in all the sediments, and higher than $[Ca]_{oxide}$ at low and medium salinity. The $[Mn]_{oxide}/[Mn]_{bulk}$ is in the range of 20.0 to 32.3% (except for 85MUC at 6.0% and 41MUC at 60.4%). For $[Al]_{oxide}$, the values range from 0.08 to 0.22 mg/g and show no clear trend with salinity in the offshore transect or with distance from the river mouth in the alongshore transect.

S2.5 Clay phase

In the clay phase of most of the MUC and SPM samples (except for 41MUC), Fe and Al are the dominant cations (Fig. S2). The clay leachate of sediment 41MUC also shows a high $[Ca]_{clay}$ of 5.78 mg/g, whereas in the other samples the $[Ca]_{clay}$ is lower and stable at around 0.35 mg/g, except for slightly higher values in 117MUC (0.62 mg/g). Except for 41MUC, $[Fe]_{clay}$ increases from 2.04 to 3.39 mg/g at the beginning of the Amazon north channel transect,

then increases slightly to 4.29 mg/g, and it fluctuates at 3.7–5.0 mg/g in the alongshore transect. For $[Al]_{clay}$, the riverine endmember of the north channel transect has 0.57 mg/g, and it then varies from 0.94 to 1.25 mg/g in the other sediments. Both $[Mg]_{clay}$ and $[K]_{clay}$ in the north channel transect increase continuously with salinity, from 0.09 to 0.49 mg/g, and from 0.02 to 0.13 mg/g, respectively.

S2.6 Residue and bulk sediments

The concentrations of Ca, Mg, K, Fe, Mn, Al and Li in the bulk sediments are calculated using Eq. (2) in the main text. Among these elements, the $[Al]_{bulk}$ is highest, followed by $[Fe]_{bulk}$, $[K]_{bulk}$, $[Mg]_{bulk}$, $[Ca]_{bulk}$ and $[Mn]_{bulk}$. In the north channel transect, the $[Ca]_{bulk}$ is 6.87 mg/g in the river endmember, remains stable at around 4.5 mg/g at low and medium salinity, and increases to 197 mg/g in the carbonate-dominated sediment 41MUC. In contrast, in that same transect, the $[Fe]_{bulk}$, $[Al]_{bulk}$, $[Mg]_{bulk}$ and $[K]_{bulk}$ increase in the low salinity zone, and then remain relatively constant at around 1.6 times the river endmember at medium salinity, before decreasing at high salinity.

S3. Cation retention by oxides

Except for sample 41MUC, which contains 39.7% carbonate (Supplementary Material S2), Fe, Mn and Al dominate the oxide leachates of the MUC and SPM samples (Fig. S2). This observation indicates that the HH leaching probably attacked Fe/Mn oxides (e.g., ferrihydrite, lepidocrocite, goethite and pyrolusite) and Al oxides (i.e., gibbsite), as expected (Velde, 1995; Bigham et al., 2002; Poulton and Canfield, 2005; Lenstra et al., 2021; Liu et al., 2022). Except

for sample 41MUC, the $[Fe]_{oxide}$ in the other leachates shows a positive relationship with $[Li]_{oxide}$ (Fig. S4). In contrast, $[Mn]_{oxide}$ and $[Al]_{oxide}$ are generally constant through the estuary and do not show clear relationships with $[Li]_{oxide}$ (Fig. S4). The different trends between $[Fe]_{oxide,}$ $[Mn]_{oxide}$ and $[Al]_{oxide}$ may imply that there is less formation of Mn-oxides (e.g., Mn-nodules, pyrolusite or birnessite) and Al-oxides (i.e., gibbsite), and more formation of Fe-oxides (e.g., ferrihydrite, lepidocrocite and goethite) through the Amazon estuary. Such a scenario seems reasonable because Fe removal in estuaries is regarded as highly related to flocculation (Boyle et al., 1977; Sholkovitz et al., 1978), whereas Mn cycling is more closely related to redox conditions (Sholkovitz, 1978; Chester, 1990). In addition, Fe removal in the estuary could also be due to Fe-rich clay formation (Michalopoulos and Aller, 1995). Furthermore, $[Mg]_{oxide}$ also increases through the estuary and shows a positive linear relationship with $[Li]_{oxide}$, while the $[Mg]_{oxide}/[Li]_{oxide}$ ratio is the same as in the clay phase (Fig. 8 in main text and Fig. S4). Since Amazon sediments contain more secondary clays than secondary oxides (Martinelli et al., 1993), the oxide leachates may be additionally influenced by inadvertent leaching of the clay or residue (Liu et al., 2022).

S4. Fractionation model for Li removal from the dissolved load into sediments

As discussed in Section 5.1.2, the exchangeable, oxide and clay phases of the sediments appear to remove Li from the saline water in the Amazon estuary with an accompanying isotopic fractionation. In the dissolved load, $[Li]_{measured}$ generally shows conservative mixing, but the measured lithium isotopic compositions ($\delta^7Li_{measured}$) are slightly higher than predicted for conservative mixing ($\delta^7Li_{conservative}$), especially at medium salinity.

Here, Rayleigh models (Eq. (S1)) and batch models (Eq. (S2)) are fitted to explore the influence of sediment Li uptake from the dissolved load (Dellinger et al., 2015; Murphy et al., 2019; Pogge von Strandmann et al., 2019a; Yang et al., 2021).

$$\delta^7Li_{after\text{-}removal} = \delta^7Li_{conservative} + 1000 \times (\alpha - 1) \times \ln(f) \quad (S1)$$

$$\delta^7Li_{after\text{-}removal} = \delta^7Li_{conservative} + 1000 \times \ln(\alpha) \times (f - 1) \quad (S2)$$

$$[Li]_{after\text{-}removal} = [Li]_{conservative} \times f \quad (S3)$$

The terms $[Li]_{conservative}$ and $\delta^7Li_{conservative}$ are the Li concentration and Li isotope composition in the dissolved load calculated based on conservative mixing. Because the measured dissolved Li concentrations conform to conservative mixing, the $[Li]_{conservative}$ here is the same as $[Li]_{measured}$ in Eq (4) in the main text. In the model, six $[Li]_{conservative}$ points are designated as 4.99 μg/L (sample W70), 10.99 μg/L (sample W69), 33.96 μg/L (sample W80), 49.10 μg/L (sample W79), 99.11 μg/L (sample W75) and 150.65 μg/L (sample W56fish) (Table S4), based on the Li concentrations in the dissolved load in the south channel transect. The terms $[Li]_{after\text{-}removal}$ and $\delta^7Li_{after\text{-}removal}$ are the Li concentration and Li isotope composition in the dissolved load after Li removal by sediments, and α is the fractionation factor between specific sediment phases and seawater. As outlined in Section 5.1.2, the leachate data indicate that $\alpha_{exchangeable\text{-}seawater}$ is approximately 0.9860–0.9935 and $\alpha_{oxide/clay\text{-}seawater}$ is approximately 0.9714–0.9757. Therefore, in the following modelling, $\alpha_{exchangeable\text{-}seawater}$ is set as 0.9900 ± 0.0050 and $\alpha_{oxide\text{-}seawater}$ and $\alpha_{clay\text{-}seawater}$ are set as 0.9750 ± 0.0050 (Table S4). These α values are similar to, or slighter smaller than, reported in previous studies (Pistiner and Henderson, 2003; Chan and Hein, 2007; Pogge von Strandmann et al., 2008, 2019a, 2020; Wimpenny et al., 2010; Hindshaw et al., 2018; Li and Liu, 2020; Li et al., 2020). The term f is the fraction of Li that

remains in the dissolved load after removal into the solid phases, and is calculated from Eq. (S4).

$$f = 1 - \mathrm{SSC} \times [\mathrm{Li}]_{\text{sediment added}} / [\mathrm{Li}]_{\text{conservative}} \quad \text{(S4)}$$

Here, SSC is the suspended sediment concentration, and $[\mathrm{Li}]_{\text{sediment added}}$ is the mass of Li per gram that is gained by the sediments.

In the Amazon estuary, the SSC in the surface layer (<3 m) is greater than 0.2 g/L just off the river mouth, greater than 0.5 g/L in the muddy area in the middle of the estuary, but less than 0.1 g/L towards the end of the estuary (Gibbs, 1976; Kineke et al., 1996). The average SSC in the Amazon river estuary has also been calculated as 0.19 g/L based on the Amazon river annual discharge of water and its particle load (Gaillardet et al., 1999; Milliman and Farnsworth, 2011). The SSC of samples SPM27–31 range from 0.26 g/L to 0.59 g/L (Table S2). To explore the influence of the SSC, the value of SSC is set at three levels: 0.1, 0.5 and 1.0 g/L (Table S4).

In the Amazon north channel transect, the maximum Li added to the estuarine sediments compared to the riverine endmember (i.e., $[\mathrm{Li}]_{\text{sediment added}}$) is 0.23 μg/g in exchangeable phases, 0.32 μg/g in oxide phases, and 0.67 μg/g in clay phases. According to the two sediment samples from the Amazon south channel transect (i.e., 67MUC and 73MUC), the sediments take up 0.18 μg/g in exchangeable phases, 0.11 μg/g in oxide phases, and 0.38 μg/g in clay phases. For the alongshore transect, the maximum Li added to the sediments (relative to the river endmember) is 0.26 μg/g in exchangeable phases, 0.33 μg/g in oxide phases, and 1.02 μg/g in clay phases. However, because the clay leaching method is designed to obtain the Li isotope composition of the clay phase rather than to quantitatively leach the entire clay phase (Liu et

al., 2022; Pogge von Strandmann et al., 2022), the amount of Li removed into the clay phase may be underestimated in this case. According to mineralogical studies, clay minerals could account for up to 50% of the Amazon river sediments (Martinelli et al., 1993). However, the residue after the clay leaching shows stable $\delta^7Li_{residue}$ values through the estuary (Fig. 9 in main text), so the residue appears to be negligibly influenced by the clay that is remaining after clay extraction. Based on mass balance considerations, the Li from any remaining clays should represent less than 20% of the total Li in the bulk sediments; otherwise, the δ^7Li values in the residue should be observed to increase with salinity, in a similar manner to the clay leachates, which is not seen. Therefore, we consider that the $[Li]_{sediment\ added}$ could potentially comprise up to a maximum of 10 μg/g. Thus, $[Li]_{sediment\ added}$ in the exchangeable phases is set as 0.2 and 0.3 μg/g (Table S4). Because of their similar fractionation factors, the oxide and clay phases can be treated as one phase with $[Li]_{sediment\ added}$ values set as 0.5, 1.0, 2.0, 5.0 and 10.0 μg/g. (Table S4).

The results of the modelling demonstrate that the Li adsorbed by the exchangeable phases rarely affects either the $[Li]_{conservative}$ or the $\delta^7Li_{conservative}$ values in the dissolved load (Table S4), while the Li removed by oxides and clay phases could increase the $\delta^7Li_{conservative}$ values without significant alteration of the $[Li]_{conservative}$ in the dissolved load. The exchangeable phases achieve a maximum adsorption of 4.2 ± 1.9% of the dissolved load Li at very low $[Li]_{conservative}$ of 5 ng/g (assuming water density as 1 g/mL), and as a result the δ^7Li value in the dissolved load can only increase by 0.28 ± 0.25‰. At a higher salinity (higher dissolved Li concentration), exchangeable phases scavenge less than 3%, and generally less than 1%, of the Li from the dissolved load. This relatively small amount of Li uptake leads to very little increase (less than

0.3‰) in the dissolved δ^7Li values. Thus, due to the relatively small amount of Li removal and the modest isotopic fractionation, the exchangeable phase negligibly changes the dissolved Li behaviour, and hence there is no discernible deviation from conservative mixing (Fig. 2 in main text).

In contrast, due to the large isotopic fractionation ($\alpha_{clay/oxide\text{-}seawater}$ = 0.9750 ± 0.0050), dissolved δ^7Li values can be increased by 2.0–3.2‰ by oxide/clay uptake if *f* is 0.90 (i.e., 10% removal), and by 4.0–6.7‰ if *f* is 0.80 (i.e., 20% removal). However, the observed conservative mixing for dissolved Li concentrations in the Amazon estuary provides a constraint on *f*, which has to remain higher than 0.95 (based on the analytical uncertainty of the Li concentrations). Thus, dissolved δ^7Li values could be increased by 1.0–1.5‰ by oxide/clay uptake, when *f* is 0.95 (Table S4, Fig. 5 in main text), which may explain the higher measured dissolved δ^7Li values in the medium salinity zone than those calculated based on conservative mixing.

In the modelling, the key controlling factors on *f* are $[Li]_{sediment\ added}$ and SSC. For Li removal by oxides/clays, when the SSC is 0.1 g/L, and $[Li]_{sediment\ added}$ is 0.5 or 1 μg/g, the value of *f* at all modelled salinity values is higher than 0.98, which causes less than a 0.6‰ increase in dissolved load δ^7Li values (Table S4, Fig. 5 in main text). In contrast, if SSC is 1 g/L and $[Li]_{sediment\ added}$ is 5 or 10 μg/g, the value of *f* is less than 0.50 in the low salinity zone, and around 0.80 at medium salinity. In that case, there would be significant Li uptake, and the mixing of dissolved Li would be readily observed as non-conservative. According to our dissolved Li data from the Amazon, at very low salinity (0–0.5), the Li concentrations and isotopes show conservative mixing (Fig. 5b in main text), consistent with little resolvable Li uptake by particles. Similarly, at low salinity (1–7), no significant Li isotopic fractionation is observed,

although Li removal could be relatively greater with *f* being 0.99 to 0.98 with approximately 0.2 g/L SSC (Gibbs, 1976) and 1–2 μg/g $[Li]_{sediment\ added}$. At medium salinity (9–18), $\delta^7Li_{measured}$ values are 1–2‰ higher than expected for conservative mixing (Fig. 5b in main text). Such values could arise in a scenario with more Li removal under conditions of 0.5g/L SSC (Gibbs, 1976) and 4–5 μg/g $[Li]_{sediment\ added}$, enabling a lowering of *f* to 0.95 (remaining consistent with the concentration data). At higher salinity (> 20), due to the high dissolved Li concentrations and lower SSC, the amount of particle Li uptake could only comprise a relatively small fraction of the Li budget, and does not cause resolvable Li isotope fractionation. Overall, for the Amazon estuary as a whole, based on the assumption that 70% of the river-derived particles are deposited on the seafloor within 200 km from the river mouth (corresponding to sample 85MUC from the Amazon north channel and W79 from the Amazon south channel at medium salinity) (Kineke et al., 1996), we estimate that the average $[Li]_{sediment\ added}$ is 3–4 μg/g.

S5. Estuary model for estimating the Li removal flux during estuarine processes

The conservative mixing model (Section 5.1.1) and fractionation model (Section 5.1.3 and Supplementary Material S4) are combined to quantify the fate of dissolved Li in the entire Amazon estuary. Here, the estuary is assumed to be at steady state, with the exchange of material (i.e., water and particles) between the river, estuary, and ocean being stable with time, and the geochemistry and particle distribution remaining constant with time. For the dissolved load in the estuary, the inputs of dissolved Li are from river water, seawater, and sediment dissolution (Fig. 6 in main text). However, the sediment samples indicate a net Li output rather than Li input. Therefore, the input from sediment/mineral dissolution cannot be directly

quantified, and can be regarded as being offset by the removal. Note that, in basalt weathering experiments, only ~4% of the Li removed by secondary mineral formation was added by primary mineral dissolution (Pogge von Strandmann et al., 2019a), which suggests that the removal process may typically be dominant. The volume of river water ($V_{riverwater}$) input is regarded as constant throughout the whole estuary, since it represents the integration of river discharge over a period of time, with the Amazon river water input being around 6300 km^3 per year (Milliman and Farnsworth, 2011). Assuming that the Li concentration in the river water at the river mouth also remains stable, the total riverine Li input flux remains stable. In other words, the river water input is assumed to travel through the whole estuary and to mix into the body of ocean water on the shelf (Fig. 6 in main text).

Based on the mixing model, the total water volume ($V_{total} = V_{riverwater}/FV_{riverwater}$) and the seawater-contributed volume can be calculated, and both increase through the estuary (Fig. 6 in main text). Thus, the mass of Li from river water and seawater can be integrated as in Eqs. (S5) and (S6), and their ratio is as shown in Eq. (S7) (Table S5). The output of dissolved Li at steady-state arises from sediment uptake. According to the fractionation model, the fraction of Li that remains in the dissolved load after sediment uptake (f) was calculated to be 1.00, 0.98, 0.95 and 0.98 at very low, low, medium and high salinity, respectively (Table S5). Thus, the fraction of Li that remains in the dissolved load after sediment removal from the beginning of the Amazon estuary to the corresponding salinity point can be calculated as Σf (Eq. (S8)). The Σf_{river} is the fraction of Li supplied by the river water that remains in the dissolved Li supplied by the river water after Li removal by sediments accumulated to a given point in the estuary (Eq. (S9)). The $\Sigma f_{seawater}$ is the fraction of Li supplied by the seawater that remains in the

dissolved Li supplied by the seawater after Li removal by sediments accumulated to a given point in the estuary (Eq. (S10)).

$$MLi_{riverwater} = \int [Li]_{conservative} \times FLi_{riverwater}\, dv_{total} \quad (S5)$$

$$MLi_{seawater} = \int [Li]_{conservative} \times FLi_{seawater}\, dv_{total} \quad (S6)$$

$$MLi_{seawater} / MLi_{riverwater} = \frac{[Li]_{seawater}}{[Li]_{riverwater}} \times \left(\frac{V_{total} - V_{river}}{V_{river} \times \ln (V_{total}/V_{river})} - 1\right) \quad (S7)$$

$$\Sigma f = \int f \times [Li]_{conservative}\, dV_{total} \,/\, \int [Li]_{conservative}\, dV_{total} \quad (S8)$$

$$\Sigma f_{river} = \int f \times [Li]_{conservative} \times FLi_{riverwater}\, dV_{total} \,/\, \int [Li]_{conservative} \times FLi_{riverwater}\, dV_{total} \quad (S9)$$

$$\Sigma f_{seawater} = \int f \times [Li]_{conservative} \times FLi_{seawater}\, dV_{total} \,/\, \int [Li]_{conservative} \times FLi_{seawater}\, dV_{total} \quad (S10)$$

In the above equations, $MLi_{riverwater}$ and $MLi_{seawater}$ represent the mass of Li discharged by the river and the mass of Li from seawater participating in the conservative mixing. The terms $[Li]_{measured}$, $[Li]_{riverwater}$, $[Li]_{seawater}$, $FLi_{riverwater}$, $FLi_{seawater}$, V_{total}, $V_{riverwater}$, and $V_{seawater}$ are described in the conservative mixing calculation (Section 5.1.1). Here, Σf, Σf_{river} and $\Sigma f_{seawater}$ were calculated using a rectangular numerical integration method. To increase the accuracy of the numerical integration, the $[Li]_{conservative}$ was interpolated at every 1 μg/L from 1 to 150 μg/L (Table S5). The accuracy and precision of the rectangular numerical integration is verified based on the ratios of $MLi_{seawater}$ and $MLi_{riverwater}$, which are integrated as in Eqs (S5) and (S6) by rectangular numerical integration, being in the range from 0.9985 to 1.0000 of $MLi_{seawater}/MLi_{riverwater}$ calculated by Eq. (S7). The corresponding salinity is calculated using linear interpolation according to the $[Li]_{measured}$ between every measured samples.

Overall, these calculations indicate around 2–3% Li loss from the river water accumulated

from the beginning of the estuary to a salinity of above 9.3 in the Amazon estuary (Fig. 6 in main text and Table S5). Based on the Amazon river water discharge (~6300 km^3/yr) (Milliman and Farnsworth, 2011), and the measured dissolved Li concentration in the river water at its mouth (sample W66, 0.87 μg/L), the dissolved Li input flux from the Amazon river is 5.5×10^9 g/yr. Therefore, the Li loss from river water in the Amazon estuary is calculated to be around $1.1–1.7\times10^8$ g/yr, equivalent to 2–3% of the Amazon river dissolved Li flux.

From the sediment perspective, the total Li uptake by the sediment (Flux $Li_{sediment\ removal}$) can be calculated from Eq. S11. Here, the $Load_{river\ sediment}$ is the sediment mass transported by river water in a given time (i.e., erosion rate if calculated based on SSC) and assumed to be deposited only in the estuary area. The average $[Li]_{sediment\ added}$ is estimated to be 3–4 μg/g based on the fractionation model (Supplementary Material S4) and the Amazon sediment load is around 1.2×10^{12} kg/yr (Milliman and Farnsworth, 2011). Therefore, the total flux of dissolved Li removed by sediment in the Amazon estuary is $3.6–4.8\times10^9$ g/yr.

$$\text{Flux } Li_{sediment\ removal} = Load_{river\ sediment} \times [Li]_{sediment\ added} \quad \text{(S11)}$$

If there is a simple mass balance in the estuary as a whole, the Li loss from the dissolved load (i.e., river water and seawater) should be equal to the Li gain in the sediment load. The Li removal mainly occurs at the beginning and middle of the estuary (Supplementary Material S4). According to Eq. (S7), integration of the seawater Li mass is ~36 times the river water Li mass from the river mouth to the middle of the estuary at a salinity of 9.3 (Fig. 6b, Table S5). In this case, around $1.0–1.3\times10^8$ g/yr of the Li uptake by sediment is from river water, which is around 1.8–2.4% of the dissolved Li flux of the Amazon river. More significantly, around $3.5–4.7\times10^9$ g/yr Li is removed from seawater by estuarine sediments in the Amazon estuary.

S6. Mineral stability and saturation

In estuaries, the mixing of river water and saline water leads to significant changes in the weathering environments for the particle loads transported by rivers, including changes in mineral saturation states. For example, the Amazon dissolved load samples show that the concentrations of Cl, Na, Mg, Ca and K rapidly increase, while the concentrations of dissolved SiO_4^{4-} and total dissolved nitrogen decrease (Table 1 in main text). Furthermore, the pH increases from around 7 in the river, to around 8.5 at medium salinity, and then decreases slightly to around 8.2 at high salinity. In this case, the predominant weathering products of feldspar shift from the kaolinite field (river) to the mica field (estuary) in the theoretical stability diagram (Fig. S3) (Tardy, 1971). The stability diagrams were plotted by PhreePlot (Kinniburgh and Cooper, 2011), with the database from PHREEQC (Parkhurst and Appelo, 2013) and Robie and Hemingway (1995). Compared to kaolinite ($Al_2Si_2O_5(OH)_4$), mica ($KAl_2[AlSi_3O_{10}](OH)_2$ or $NaAl_2[AlSi_3O_{10}](OH)_2$) could retain more cations (e.g., Na, K, Mg, Li).

Using PHREEQC (Parkhurst and Appelo, 2013), the saturation index (SI) for a range of minerals was calculated using input concentrations of Na, Ca, Mg, K, Li, NO_2^-, SiO_4^{4-}, NO_3^- and Cl^-, and alkalinity, temperature and pH (Table S6). As expected, carbonate minerals, such as calcite, aragonite and dolomite, rapidly shift from being undersaturated in the river water to being supersaturated in the saline water (Fig. S5). Salts (i.e., halite and sylvite) are undersaturated in the whole estuary, although their SI also increases with increasing salinity. Most importantly, the calculations show that silicate minerals, such as sepiolite and talc, are

highly supersaturated, with their SI increasing from around 10 in the river water to 17 at low to medium salinity and then decreasing slightly to around 14 at high salinity (Fig. S5). These calculated SIs support the removal of cations such as Mg and Li into sediment particles in the estuary.

S7. List of symbols in the modelling

$[Li]_{measured}$: Li concentration of each dissolved sample measured by ICP-MS.

$\delta^7Li_{measured}$: Li isotope composition of each dissolved sample measured by MC-ICP-MS.

$[Li]_{riverwater}$: Li concentration of Amazon river water at the estuary, i.e., the Li concentration of sample W66.

$\delta^7Li_{riverwater}$: Li isotope composition of Amazon river water at the estuary, i.e., the Li isotope composition of sample W66.

$[Li]_{seawater}$: Li concentration of modern seawater, i.e., 180 μg/L.

$\delta^7Li_{seawater}$: Li isotope composition of modern seawater, i.e., 31‰.

V_{river}: volume of Amazon river water contributed during conservative mixing based on Li concentration.

$V_{seawater}$: volume of seawater contributed during conservative mixing based on Li concentration.

V_{total}: total volume of water from mixing of river water and seawater.

$FV_{riverwater}$: mass fraction of the water volume contributed by Amazon river water

$FV_{seawater}$: mass fraction of the water volume contributed by seawater, assuming a density of seawater approximately equal to river water.

$FLi_{riverwater}$: mass fraction of the Li contributed by Amazon river water.

$F\mathrm{Li}_{seawater}$: mass fraction of the Li contributed by seawater.

$\delta^7\mathrm{Li}_{conservative}$: dissolved Li isotope composition in the estuary that would be expected based on theoretical conservative mixing of river water and seawater.

$[\mathrm{Li}]_{conservative}$: Li concentration in the dissolved load based on conservative mixing of river water and seawater. It is the same as $[\mathrm{Li}]_{measured}$ at the measured sample points.

$[\mathrm{Li}]_{after\text{-}removal}$: Li concentration in the dissolved load after Li removal by sediments.

$\delta^7\mathrm{Li}_{after\text{-}removal}$: Li isotope composition in the dissolved load after Li removal by sediments.

f: fraction of Li that remains in the dissolved load after Li removal by sediments.

$[\mathrm{Li}]_{sediment\ added}$: the mass of Li per gram that is gained by sediments in the estuary.

SSC: suspended sediment concentration.

α: Li isotopic fractionation factor.

$\mathrm{Load}_{river\ sediment}$: mass per unit time of sediment transported by river water to the estuary (i.e., erosion rate if it is calculated based on the SSC in the river water).

Flux $\mathrm{Li}_{sediment\ removal}$: the flux of Li (mass) removed in the estuary by the river-transported sediments.

$\mathrm{MLi}_{riverwater}$: accumulated mass of Li supplied by the river water to a given point during the conservative mixing of river water and seawater.

$\mathrm{MLi}_{seawater}$: accumulated mass of Li supplied by the seawater to a given point during the conservative mixing of river water and seawater.

Σf: fraction of Li that remains in the dissolved load after Li removal by sediments accumulated to a given point in the estuary.

Σf_{river}: fraction of Li supplied by the river water that remains in the dissolved Li supplied by

the river water after Li removal by sediments accumulated to a given point in the estuary.

$\Sigma f_{seawater}$: fraction of Li supplied by the seawater that remains in the dissolved Li supplied by the seawater after Li removal by sediments accumulated to a given point in the estuary.

References

Andrews, E., Pogge von Strandmann, P. A. E., Fantle, M. S., 2020. Exploring the importance of authigenic clay formation in the global Li cycle. Geochim. Cosmochim. Acta 289, 47–68.

Bastian, L., Vigier, N., Reynaud, S., Kerros, M. E., Revel, M., Bayon, G., 2018. Lithium isotope composition of marine biogenic carbonates and related reference materials. Geostand. Geoanal. Res. 42, 403–415.

Baturin, G. N., Gordeev, V. V., 2019. Geochemistry of Suspended Matter in the Amazon River Waters. Geochemistry Int. 57, 197–205.

Bigham, J. M., Fitzpatrick, R. W., Schulze, D. G., 2002. Iron oxides. Soil Mineral. with Environ. Appl. 7, 323–366.

Boyle, E. A., Edmond, J. M., Sholkovitz, E. R., 1977. The mechanism of iron removal in estuaries. Geochim. Cosmochim. Acta 41, 1313–1324.

Chan, L. H., Hein, J. R., 2007. Lithium contents and isotopic compositions of ferromanganese deposits from the global ocean. Deep. Res. Part II Top. Stud. Oceanogr. 54, 1147–1162.

Chester, R., 1990. Marine Geochemistry. Unwin Hyman Ltd, London.

Dellinger, M., Gaillardet, J., Bouchez, J., Calmels, D., Louvat, P., Dosseto, A., Gorge, C., Alanoca, L., Maurice, L., 2015. Riverine Li isotope fractionation in the Amazon River basin controlled by the weathering regimes. Geochim. Cosmochim. Acta 164, 71–93.

Dellinger, M., Hardisty, D. S., Planavsky, N. J., Gill, B. C., Kalderon-Asael, B., Asael, D., Croissant, T., Swart, P. K., West, A. J., 2020. The effects of diagenesis on lithium isotope ratios of shallow marine carbonates. Am. J. Sci. 320, 150–184.

Gaillardet, J., Dupré, B., Louvat, P., Allègre, C. J., 1999. Global silicate weathering and CO_2

consumption rates deduced from the chemistry of large rivers. Chem. Geol. 159, 3–30.

Gibbs, R. J., 1967. The Geochemistry of the Amazon River System: Part I. The Factors that Control the Salinity and the Composition and Concentration of the Suspended Solids. GSA Bull. 78, 1203–1232.

Gibbs, R. J., 1976. Amazon River sediment transport in the Atlantic Ocean. Geology 4, 45–48.

Hindshaw, R. S., Aciego, S. M., Tipper, E. T., 2018. Li and U isotopes as a potential tool for monitoring active layer deepening in permafrost dominated catchments. Front. Earth Sci. 6, 102.

Kinniburgh, D., Cooper, D., 2011. PhreePlot: Creating graphical output with PHREEQC.

Kineke, G. C., Sternberg, R. W., Trowbridge, J. H., Geyer, W. R., 1996. Fluid-mud processes on the Amazon continental shelf. Cont. Shelf Res. 16, 667–696.

Koschinsky, A., Frank, M., Dittmar, T., Gledhill, M., de Rezende, C., Lodeiro, P., Seidel, M., Knoke, M., Paul, S., Zitoun, R., Heinrich, L., Fronzek, J., Münch, J., Scholten, J., Border, E., Schneider, A., de Carvalho, L., Leist, L., Mutzberg, A., Marques da Silva Jr., J., Cherene Bras de Oliveira, B., Walter, J., Soares Nóbrega, M., Bretschneider, L., Hathorne, E., Vosteen, P., Spiegel, T., Maguire, C., Rohleder, C., 2018. Interactions of trace metals, DOM, and particles in the Amazon estuary and associated plume as key processes for trace metal and DOM fluxes into the Atlantic. A contribution to the internatinal GEOTRACES program Cruise No. M147.

Kuehl, S. A., Nittrouer, C. A., DeMaster, D. J., 1982. Modern sediment accumulation and strata formation on the Amazon continental shelf. Mar. Geol. 49, 279–300.

Lenstra, W. K., Klomp, R., Molema, F., Behrends, T., Slomp, C. P., 2021. A sequential extraction procedure for particulate manganese and its application to coastal marine sediments.

Chem. Geol. 584, 120538.

Li, W., Liu, X. M., 2020. Experimental investigation of lithium isotope fractionation during kaolinite adsorption: Implications for chemical weathering. Geochim. Cosmochim. Acta 284, 156–172.

Li, W., Liu, X. M., Chadwick, O. A., 2020. Lithium isotope behavior in Hawaiian regoliths: Soil-atmosphere-biosphere exchanges. Geochim. Cosmochim. Acta 285, 175–192.

Liu, C. Y., Pogge von Strandmann, P. A. E., Tarbuck, G., Wilson, D. J., 2022. Experimental investigation of oxide leaching methods for Li isotopes. Geostand. Geoanal. Res. 46, 493–518.

Martinelli, L. A., Victoria, R. L., Dematte, J. L. I., Richey, J. E., Devol, A. H., 1993. Chemical and mineralogical composition of Amazon River floodplain sediments, Brazil. Appl. Geochemistry 8, 391–402.

Michalopoulos, P., Aller, R. C., 1995. Rapid clay mineral formation in Amazon delta sediments: Reverse weathering and oceanic elemental cycles. Science 270, 614–617.

Milliman, J. D., Farnsworth, K. L., 2011. River discharge to the coastal ocean: A global synthesis. Cambridge University Press. New York.

Misra, S., Froelich, P. N., 2012. Lithium isotope history of cenozoic seawater: Changes in silicate weathering and reverse weathering. Science 335, 818–823.

Murphy, M. J., Porcelli, D., Pogge von Strandmann, P. A. E., Hirst, C. A., Kutscher, L., Katchinoff, J. A., Mörth, C. M., Maximov, T., Andersson, P. S., 2019. Tracing silicate weathering processes in the permafrost-dominated Lena River watershed using lithium isotopes. Geochim. Cosmochim. Acta 245, 154–171.

Parkhurst, D. L., Appelo, C. A. J., 2013. Description of input and examples for PHREEQC

version 3—A computer program for speciation, batch-reaction, one-dimensional transport, and inverse geochemical calculations. US Geol. Surv. Tech. methods 6, 497.

Pistiner, J. S., Henderson, G. M., 2003. Lithium-isotope fractionation during continental weathering processes. Earth Planet. Sci. Lett. 214, 327–339.

Pogge von Strandmann, P. A. E., James, R. H., van Calsteren, P., Gíslason, S. R., Burton, K. W., 2008. Lithium, magnesium and uranium isotope behaviour in the estuarine environment of basaltic islands. Earth Planet. Sci. Lett. 274, 462–471.

Pogge von Strandmann, P. A. E., Jenkyns, H. C., Woodfine, R. G., 2013. Lithium isotope evidence for enhanced weathering during Oceanic Anoxic Event 2. Nat. Geosci. 6, 668–672.

Pogge von Strandmann, P. A. E., Fraser, W. T., Hammond, S. J., Tarbuck, G., Wood, I. G., Oelkers, E. H., Murphy, M. J., 2019a. Experimental determination of Li isotope behaviour during basalt weathering. Chem. Geol. 517, 34–43.

Pogge von Strandmann, P. A. E., Schmidt, D. N., Planavsky, N. J., Wei, G., Todd, C. L., Baumann, K. H., 2019b. Assessing bulk carbonates as archives for seawater Li isotope ratios. Chem. Geol. 530, 119338.

Pogge von Strandmann, P. A. E, Dellinger, M., West, A. J., 2021. Lithium Isotopes: A Tracer of Past and Present Silicate Weathering, in: Lyons, T., Turchyn, A., Reinhaed, C. (Eds.), Geochemical Tracers Earth System Science. Cambridge University Press, Cambridge, pp. 1–24.

Pogge von Strandmann, P. A. E., Liu, X., Liu, C. Y., Wilson, D. J., Hammond, S. J., Tarbuck, G., Aristilde, L., Krause, A. J., Fraser, W. T., 2022. Lithium isotope behaviour during basalt weathering experiments amended with organic acids. Geochim. Cosmochim. Acta 328, 37–57.

Poulton, S. W., Canfield, D. E., 2005. Development of a sequential extraction procedure for iron: implications for iron partitioning in continentally derived particulates. Chem. Geol. 214, 209–221.

Robie, R., Hemingway, B., 1995. Thermodynamic properties of minerals and related substances at 298.15 K and 1 bar (10^5 Pascals) pressure and at higher temperatures. Bull. U.S. Geol. Surv. 2131, pp.461.

Sayles, F. L., Mangelsdorf Jr., P. C., 1979. Cation-exchange characteristics of Amazon River suspended sediment and its reaction with seawater. Geochim. Cosmochim. Acta 43, 767–779.

Sholkovitz, E. R., Boyle, E. A., Price, N. B., 1978. The removal of dissolved humic acids and iron during estuarine mixing. Earth Planet. Sci. Lett. 40, 130–136.

Sholkovitz, E. R., 1978. The flocculation of dissolved Fe, Mn, Al, Cu, Ni, Co and Cd during estuarine mixing. Earth Planet. Sci. Lett. 41, 77–86.

Smrzka, D., Zwicker, J., Bach, W., Feng, D., Himmler, T., Chen, D., Peckmann, J., 2019. The behavior of trace elements in seawater, sedimentary pore water, and their incorporation into carbonate minerals: a review. Facies 65, 41.

Spiegel, T., Vosteen, P., Wallmann, K., Paul, S. A. L., Gledhill, M., Scholz, F., 2021. Updated estimates of sedimentary potassium sequestration and phosphorus release on the Amazon shelf. Chem. Geol. 560, 120017.

Tardy, Y., 1971. Characterization of the principal weathering types by the geochemistry of waters from some European and African crystalline massifs. Chem. Geol. 7, 253–271.

Ullmann, C. V., Campbell, H. J., Frei, R., Hesselbo, S. P., Pogge von Strandmann, P. A. E., Korte, C., 2013. Partial diagenetic overprint of Late Jurassic belemnites from New Zealand:

Implications for the preservation potential of δ^7Li values in calcite fossils. Geochim. Cosmochim. Acta 120, 80–96.

Velde, B, 1995. Origin and Mineralogy of Clays. Springer, Germany.

Vosteen, P., Spiegel, T., Gledhill, M., Frank, M., Zabel, M., Scholz, F., 2022. The fate of sedimentary reactive iron at the land-ocean interface: A case study from the Amazon shelf. Geochem. Geophys., 23, e2022GC010543.

Washington, K. E., West, A. J., Kalderon-Asael, B., Katchinoff, J. A. R., Stevenson, E. I., Planavsky, N. J., 2020. Lithium isotope composition of modern and fossilized Cenozoic brachiopods. Geology 48, 1058–1061.

Wimpenny, J., Gíslason, S. R., James, R. H., Gannoun, A., Pogge von Strandmann, P. A. E., Burton, K. W., 2010. The behaviour of Li and Mg isotopes during primary phase dissolution and secondary mineral formation in basalt. Geochim. Cosmochim. Acta 74, 5259–5279.

Yang, C., Vigier, N., Lian, E., Lai, Z., Yang, S., 2021. Decoupling of dissolved and particulate Li isotopes during estuarine processes. Geochem. Perspect. Lett. 19, 40–44.

Zhang, L., Chan, L. H., Gieskes, J. M., 1998. Lithium isotope geochemistry of pore waters from Ocean Drilling Program Sites 918 and 919, Irminger Basin. Geochim. Cosmochim. Acta 62, 2437–2450.

Figures

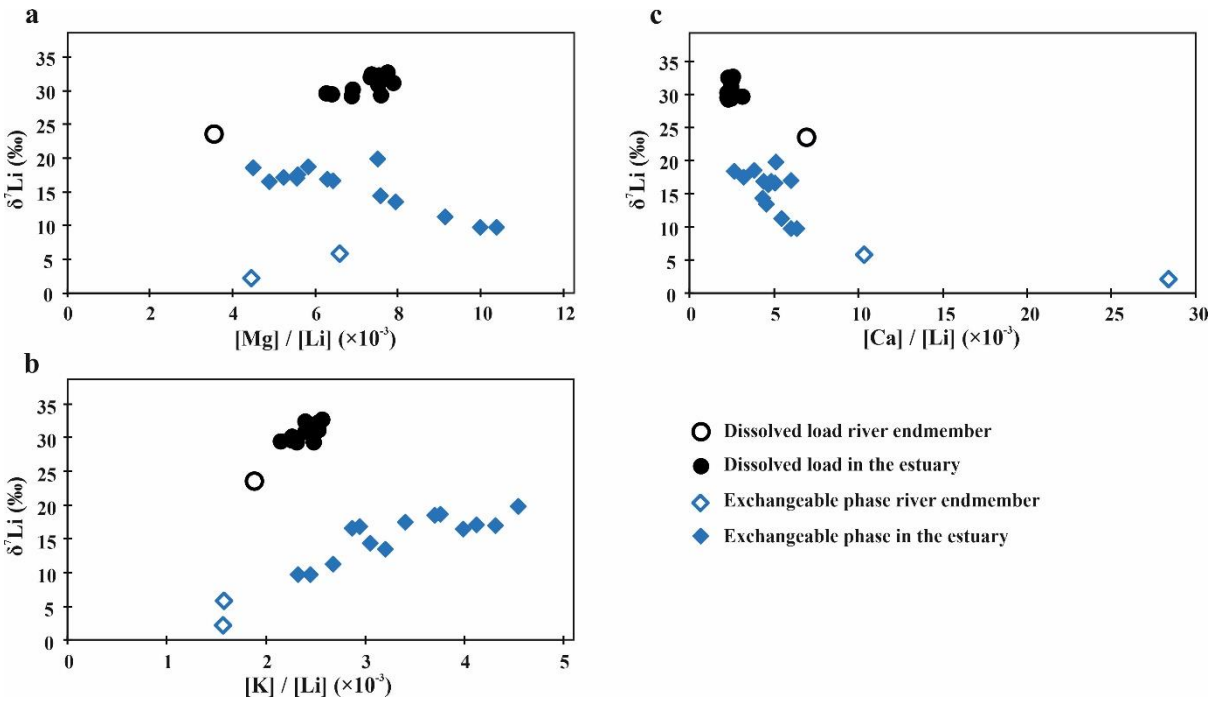

Fig. S1. Negligible influence of the remaining dissolved load on the exchangeable pool.

(a) Li isotope compositions versus Mg/Li ratios. (b) Li isotope compositions versus K/Li ratios. (c) Li isotope compositions versus Ca/Li ratios. The open black circles and open blue diamonds are the dissolved load (W66) and the exchangeable phases extracted from sediments (24MUC and 67MUC) that represent the river endmember near the beginning of the Amazon estuary. The filled black circles and filled blue diamonds represent the other samples from the Amazon estuary. The element ratios are by mass.

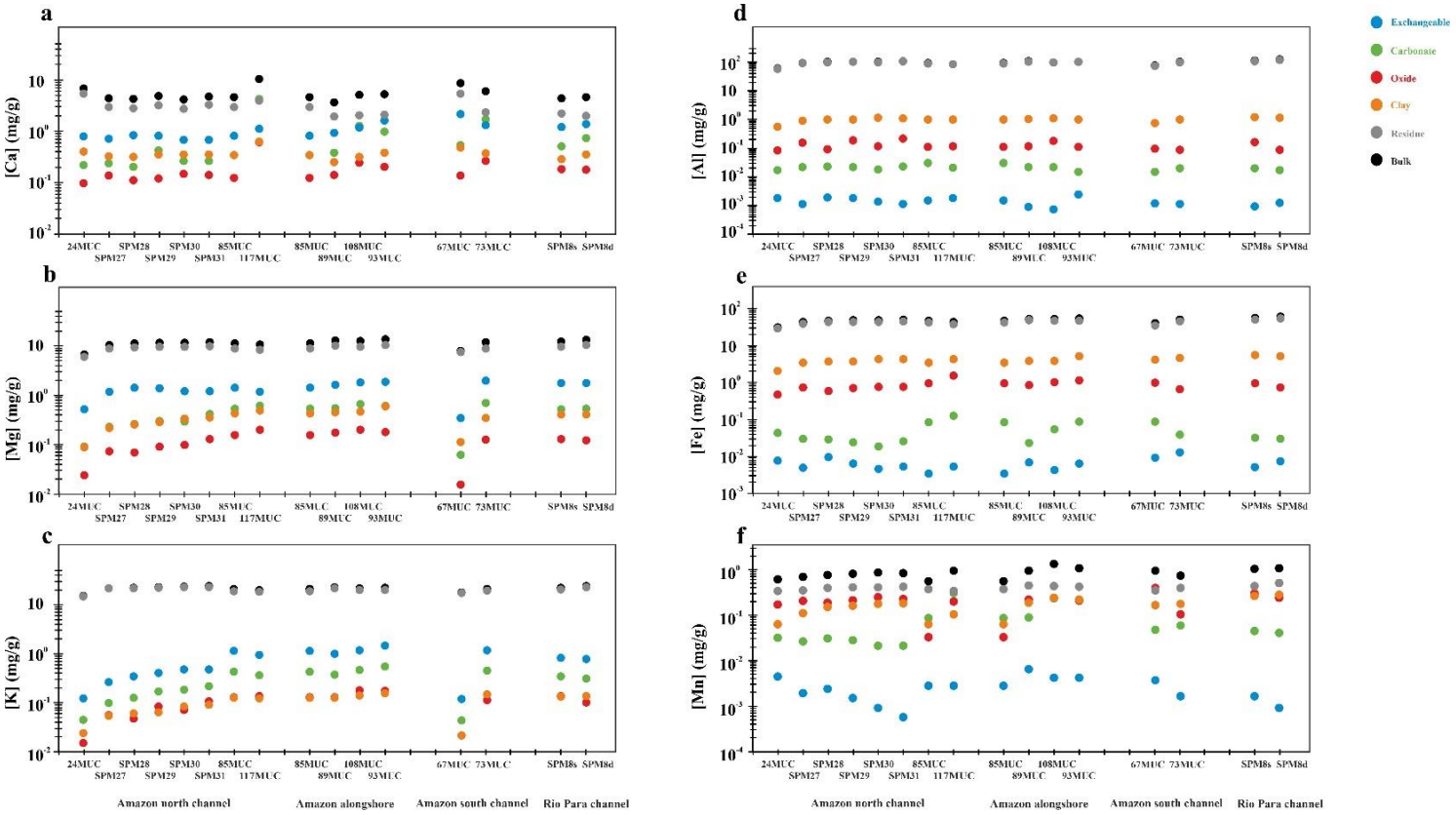

Fig. S2. Elemental concentrations for different phases of the sediment samples.

Panels (a), (b), (c), (d), (e) and (f) are the concentrations of Ca, Mg, K, Al, Fe and Mn for different phases of the sediment samples. Note that the phases are separated based on sequential leaching, and that the carbonate phase is probably influenced by the leaching of phases other than carbonate (Supplementary Material S2). The data labelled 'bulk' represent the sum of the other fractions, based on Eq. (2) in the main text. Where the black data points are not visible, they are hidden by the grey data points because of their similar values. Note that data from sample 41MUC are not shown.

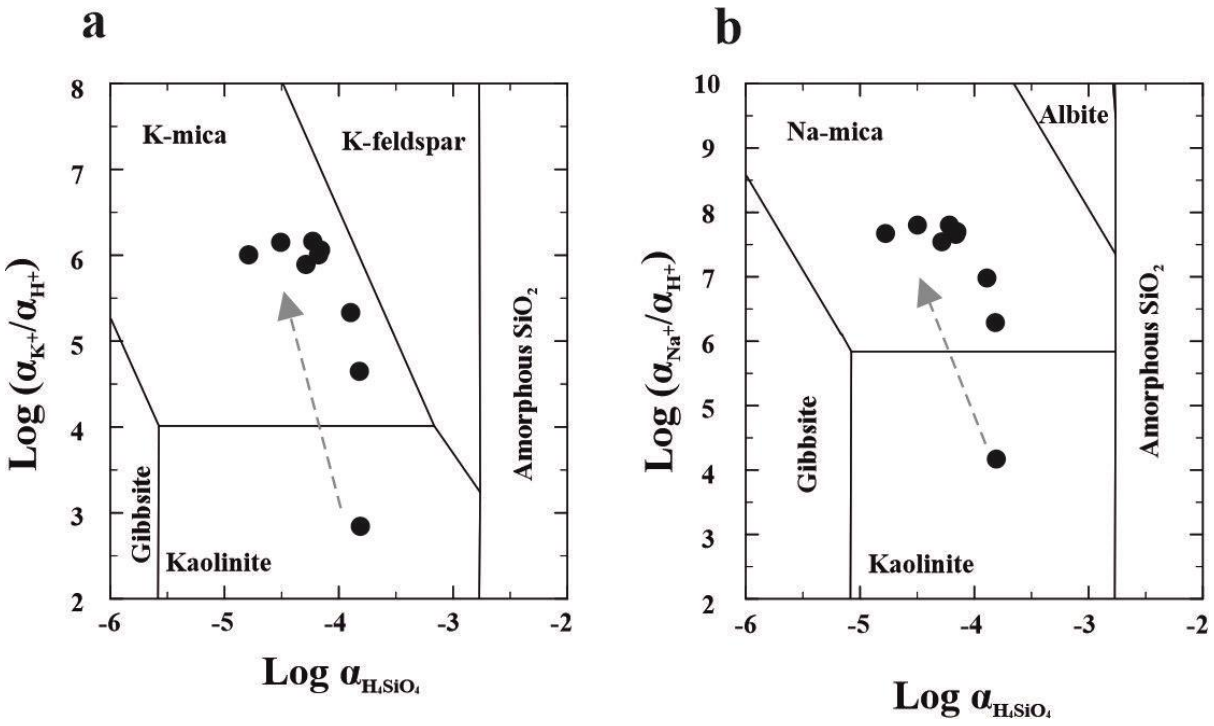

Fig. S3. Stability diagrams of K-aluminosilicate and Na-aluminosilicate.

(a) Stability diagram of K-aluminosilicate. (b) Stability diagram of Na-aluminosilicate. Calculations for individual water samples are shown as black filled circles, and the grey arrows indicate the direction from river to ocean. For details, see Supplementary Material S6.

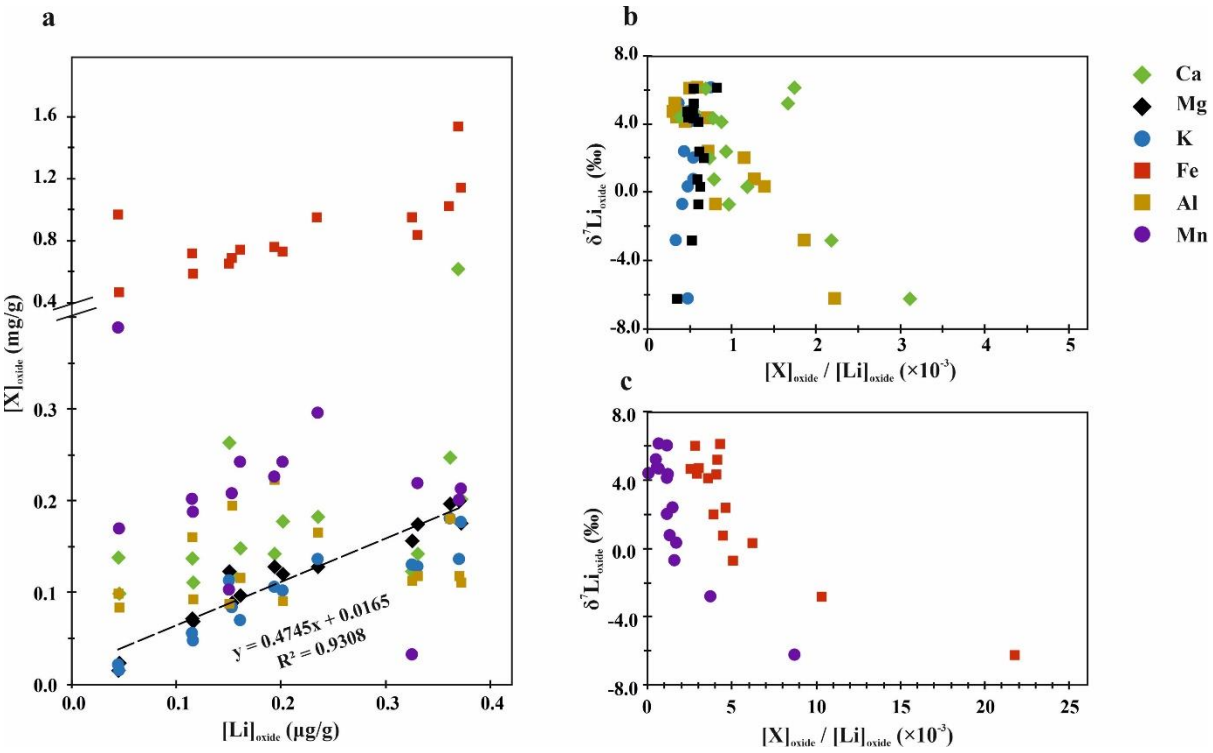

Fig. S4. The retention of cations in oxide phases.

(a) Trends of major element concentrations (Ca, Mg, K, Fe, Al, Mn) with Li concentrations in the leached oxide phase of the sediment samples, i.e., SPM and MUC (except for 41MUC). The black dashed line is a best-fit line for $[Mg]_{oxide}$ and $[Li]_{oxide}$. (b) Trends of Li isotope compositions with Ca, Mg, K and Al concentrations (plotted as ratios to Li concentrations) in the leached oxide phase of the sediment samples, i.e., SPM and MUC (except for 41MUC). (c) Trends of Li isotope compositions with Fe and Mn concentrations (plotted as ratios to Li concentrations) in the leached oxide phase of the sediment samples, i.e., SPM and MUC (except for 41MUC). The element ratios are by mass.

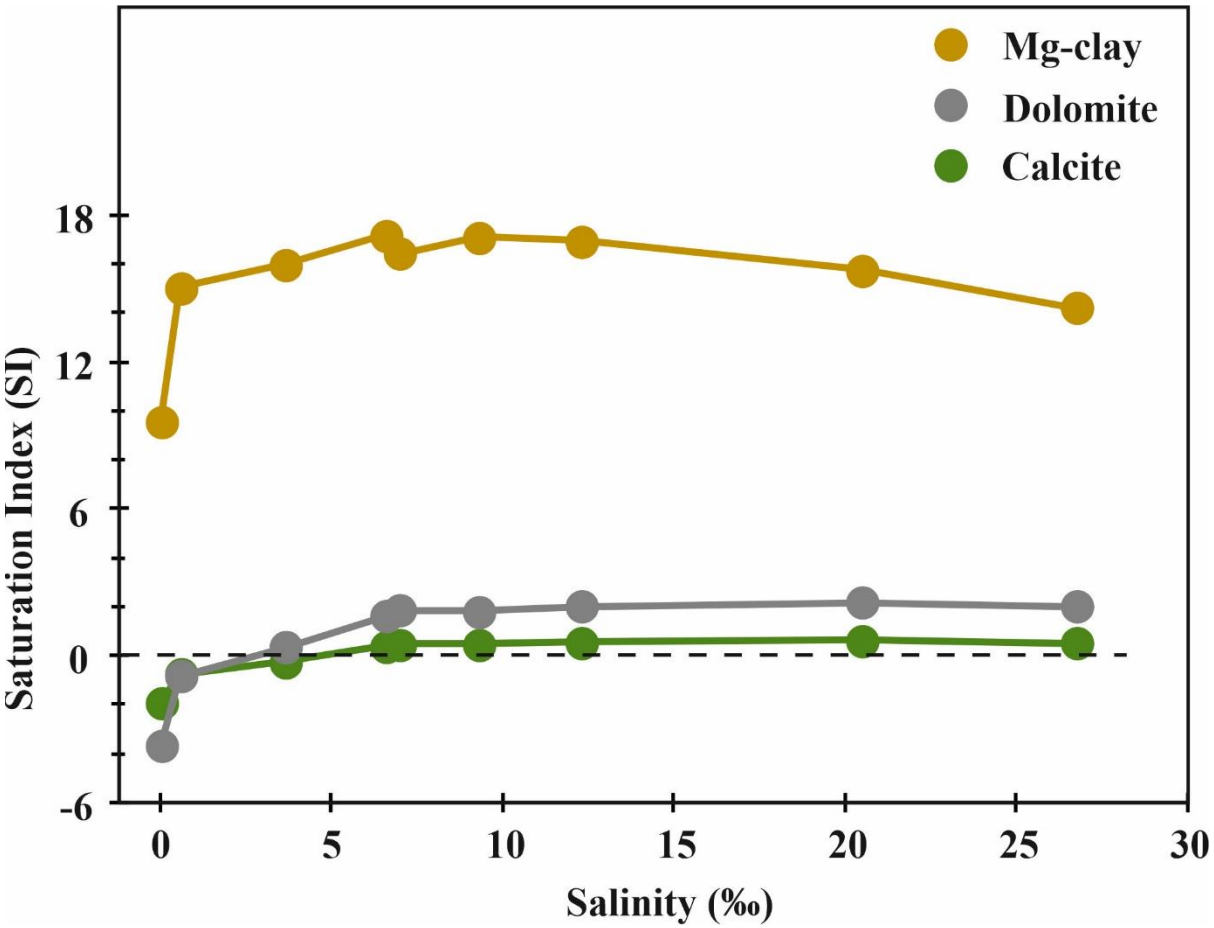

Fig. S5. Calculated saturation index (SI) for selected minerals in the Amazon estuary.

The dashed black line is plotted at SI=0; lower values are undersaturated and higher values are supersaturated. For details, see Supplementary Material S6 and Table S1. The Mg-clay here is sepiolite.

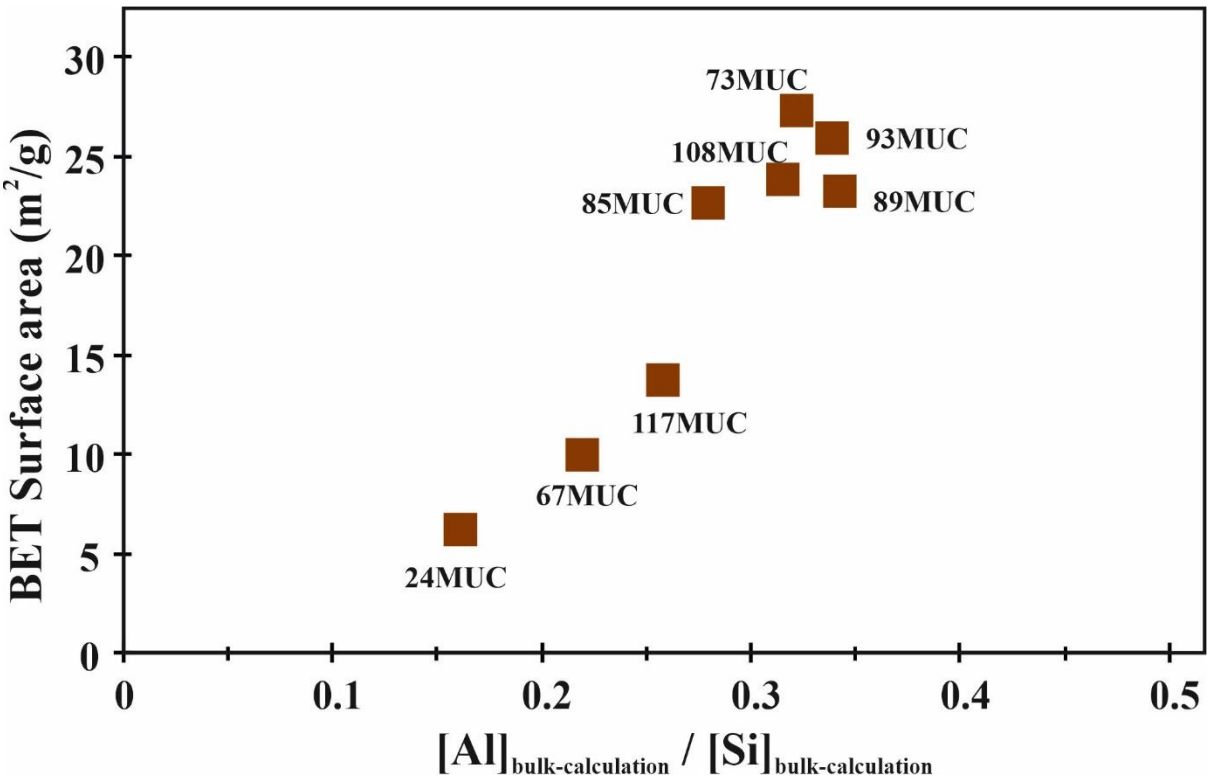

Fig. S6. Relationship between BET surface area and bulk Al/Si ratios in the MUC sediment samples.

Sample 41MUC is excluded because of its high carbonate content. The element ratios are by mass. The surface area of the MUC samples was determined by Nova 1200 (Quantachrome) at Johannes Gutenberg University, Mainz.

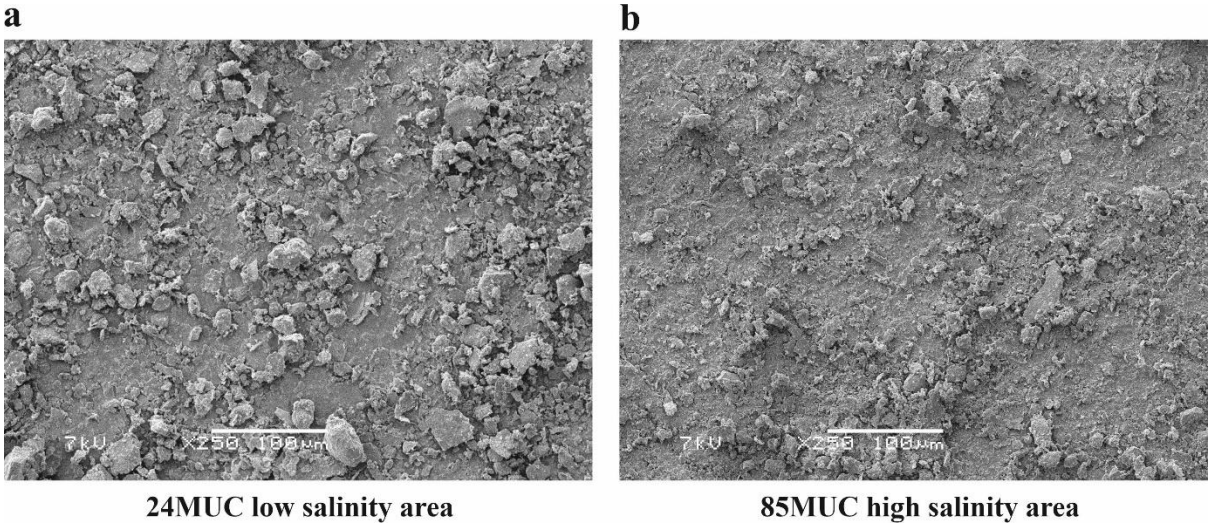

Fig. S7. SEM images for sediment samples 24MUC and 85MUC.

(a) Sample 24MUC at 50 km away from the Amazon river mouth in the estuary. (b) Sample 85MUC at around 200 km away from the Amazon river mouth in the estuary. Samples were imaged at UCL with a Jeol JSM-6480LV high-performance Variable Pressure Analytical Scanning Electron Microscope, using a 7 kV accelerating voltage and around 9 mm working distance. The scale bars are 100 μm.